PHYSICAL REVIEW E **78**, 046315 (2008)

Thermal convection in mixtures with an inversion of the separation ratio

B. Huke,[1,2] H.Pleiner,[2] and M. Lücke[1]
[1]*Institut für Theoretische Physik,Universität des Saarlandes, D-66041 Saarbrücken, Germany*
[2]*Max Planck Institute for Polymer Research, D–55021 Mainz, Germany*
(Received 14 September 2007; revised manuscript received 5 September 2008; published 29 October 2008)

We have numerically investigated Rayleigh–Bénard convection in binary mixtures assuming a thermal diffusion ratio that depends on the local temperature and changes its sign within the cell. The stationary instability has been found to precede the oscillatory one for a wide range of negative mean ψ values. The bifurcation diagram for stationary rolls turns out to be qualitatively different from that for constant Soret effect. Nevertheless, it can be mapped onto this special case by using a scaling argument, taking into account the fact that for small convection amplitudes the rolls are restricted to parts of the cell where the sign of the Soret coefficient favors instability.

PACS numbers: 47.20.Bp 47.54.-r 47.20.Ky DOI: 10.103/PhysRevE.78.046315

I. INTRODUCTION

The Rayleigh–Bénard system [1, 2] consisting of a horizontal fluid layer heated from below is one of the classical setups to study pattern formation in hydrodynamics. Especially rich bifurcation scenarios emerge when considering the convection in binary fluids [3–5] where the concentration enters the basic equations as an additional dynamic entity. The concentration field couples into the Navier–Stokes equation via the concentration dependent density in the buoyancy force term. Since advection and diffusion alone would lead to an equilibration of the concentration field leaving an effectively one–component system a back–coupling is also necessary. This back–coupling is provided by the Soret effect, the driving of concentration currents by thermal gradients.

Rayleigh–Bénard convection is typically studied within the Oberbeck–Boussinesq (OB) approximation [4, 6], where the relevant material constants are assumed to be independent of the thermodynamic variables. The exception is the density which must necessarily be temperature–dependent to allow for a convective instability. In the case of binary mixtures it must also be concentration–dependent as explained above.

Non–Oberbeck–Boussinesq effects in mixtures are less well studied [7] although they lead to qualitative changes by breaking the up–down–symmetry of the system which is known to affect the pattern selection at onset in pure fluids [8].

In the dedimensionalized OB–equations, the three dimensionless system parameters (next to the control parameter, the Rayleigh number R) are the Prandtl number σ, the Lewis number L, and the separation ratio ψ to be defined further below. Only the latter, being proportional to the strength and direction of the Soret effect can be both positive and negative. In the case of a positive separation ratio the lighter component is driven into the direction of higher temperatures, thus further enhancing the density gradient. For negative ψ, the opposite is the case.

The sign of ψ greatly affects the bifurcation behavior. Qualitative changes that happen at or close to $\psi = 0$ are for example the appearance of a bifurcation threshold for heating from above when $\psi < 0$, the appearance of a Hopf bifurcation threshold, also when $\psi < 0$, and the change of the stationary bifurcation for $R > 0$ from a forward type (for $\psi > 0$) to a backward type (for $\psi < 0$). As a consequence of these changes, convection at small Rayleigh numbers is dominated by stationary structures like roll and square patterns for positive ψ [9–15], whereas for $\psi < 0$ oscillatory structures like traveling and standing waves bifurcate first [16–23].

It is thus of particular interest to consider a system where ψ changes its sign with temperature since it should exhibit not only just quantitative differences to systems with globally constant ψ. Investigating the bifurcation properties of such a system is the goal of this paper. They can be experimentally realized. An example for a mixture in which the Soret coefficient $S_T \sim \psi$ depends strongly on temperature and changes its sign is a solution of poly(N-isopropylacrylamide) in ethanol (PNiPAM/ethanol) [24]. Polymer solutions typically possess larger separation ratios than molecular mixtures which has been explained by the large particle size [25]. In the case of PNiPAM/ethanol S_T changes by about 0.2 K^{-1} over a temperature interval of 35 K for the concentrations investigated in [24]. For comparison, in a typical molecular mixture like ethanol/water the change over the same temperature interval is about 5 10^{-4} K^{-1}, and the sign of S_T is virtually independent of temperature [26]. Strong dependence on temperature allows to study convection in cells with large differences in ψ while keeping the temperature differences and thus the temperature deviations of the other parameters small.

Our paper is organized as follows: In Sec. II we will present the basic equations of the system under consideration, calculate their conductive solution, and reformulate them into a dimensionless form. In the following section we will briefly outline the Galerkin method we used and discuss some technical details. In Sec. IV we will

investigate the linear stability of the ground state in the three important cases of stationary instability for heating from below, stationary instability for heating from above, and oscillatory instability for heating from below. In Sec. V we will extend the investigation to an important type of nonlinear solutions, namely stationary convection rolls for heating from below. Nonlinear oscillatory convection will be discussed in Sec. VI. We will summarize our findings in Sec. VII.

II. SYSTEM AND BASIC EQUATIONS

A. Basic equations

We consider a layer of a binary fluid, confined between two impermeable, parallel plates at distance d and perpendicular to the direction of gravity $\mathbf{g} = -g\mathbf{e}_z$, kept at constant temperatures.

The basic equations to describe this problem read [4]

$$\underline{d}_t\rho + \rho\nabla\cdot\underline{\mathbf{u}} = 0 \tag{2.1a}$$

$$\underline{d}_t(\rho\,\underline{\mathbf{u}}) = -\nabla\,\underline{p} + \nabla\cdot\overleftrightarrow{\sigma} - \rho\,g\,\mathbf{e}_z \tag{2.1b}$$

$$\underline{d}_t(C_p\,\underline{T}) = \nabla\cdot(\lambda\,\nabla\underline{T}) \tag{2.1c}$$

$$\underline{d}_t\underline{C} = \nabla\cdot\left[D\,(\nabla\underline{C} + \frac{k_T}{\underline{T}}\nabla\underline{T})\right] \quad . \tag{2.1d}$$

with $\underline{d}_t = \partial_t + \underline{\mathbf{u}}\cdot\nabla$. To distinguish the dimensional fields from the dimensionless counterparts introduced below we have underlined them. $\underline{\mathbf{u}}$, $\underline{T}$, $\underline{C}$, and $\underline{p}$ are respectively the velocity, temperature, concentration, and pressure of the fluid. The four equations are from top to bottom the balance equations for mass, momentum (the Navier–Stokes equation), heat, and concentration.

The first equation simply describes the conservation of mass. The relevant force densities on the right hand side of the Navier–Stokes equation are pressure gradients, friction represented by the viscous tensor $\overleftrightarrow{\sigma}$, and gravity. On the right hand sides of (2.1c) and (2.1d) there are altogether three diffusion terms, two diagonal ones and one off–diagonal in (2.1d), coupling the temperature into the dynamics of the concentration and thus representing the Soret effect. The thermal diffusion ratio k_T is related to the Soret coefficient S_T via the equation $k_T = \underline{T}\underline{C}(1-\underline{C})S_T$.

Within the OB approximation all the material constants appearing here are assumed to be indeed constant. The same holds for the density, except in the gravity term, because buoyancy effects are necessary for the backcoupling of temperature and concentration into the dynamics. The density term here is assumed to depend linearly on $\underline{T}$ and $\underline{C}$ via the thermal and solutal expansion coefficients α and β. We expand around mean values $\underline{T}_0$ and $\underline{C}_0$:

$$\rho = \rho_0\left[1 - \alpha(\underline{T}-\underline{T}_0) - \beta(\underline{C}-\underline{C}_0)\right] \quad . \tag{2.2}$$

$\underline{C}$ is chosen to be the concentration of the lighter fluid component such that β is positive. Deviating from the OB approximation we also assume a dependence of the term embodying the Soret effect on the local temperature, writing

$$\frac{k_T}{\underline{T}} = \frac{k_{T,0}}{\underline{T}_0}\left[1 + \gamma(\underline{T}-\underline{T}_0)\right] \quad . \tag{2.3}$$

It is

$$\gamma = \frac{1}{k_{T,0}}\left.\frac{\partial k_T}{\partial\underline{T}}\right|_{\underline{T}=\underline{T}_0} - \frac{1}{\underline{T}_0} \quad . \tag{2.4}$$

The term $\frac{1}{\underline{T}_0}$ stems from the linear expansion of $1/\underline{T}$. It has been included for reasons of completeness but is negligible.

Applying this modified OB approximation to the basic equations one obtains

$$\nabla\cdot\underline{\mathbf{u}} = 0 \tag{2.5a}$$

$$\underline{d}_t\underline{\mathbf{u}} = -\frac{1}{\rho_0}\nabla\,\underline{p} + \nu\nabla^2\underline{\mathbf{u}} + (\alpha\underline{T} + \beta\underline{C})\;g\,\mathbf{e}_z \tag{2.5b}$$

$$\underline{d}_t\underline{T} = \kappa\nabla^2\underline{T} \tag{2.5c}$$

$$\underline{d}_t\underline{C} = D\nabla^2\underline{C} + D\frac{k_{T,0}}{\underline{T}_0}\nabla^2\underline{T} \tag{2.5d}$$

$$+D\gamma\frac{k_{T,0}}{\underline{T}_0}\left[(\underline{T}-\underline{T}_0)\nabla^2\underline{T} + \nabla\underline{T}\cdot\nabla\underline{T}\right] \quad . \tag{2.5e}$$

The mass balance equation reduces to an incompressibility condition (2.5a), allowing us to write the friction term simply as $\nu\nabla^2\underline{\mathbf{u}}$ for a Newtonian fluid, with the kinematic viscosity ν. We have redefined the pressure, including some constant terms. $\kappa = \lambda/C_p$ is the thermal diffusivity.

B. The conductive state

We will now consider the conductive state in the Rayleigh–Bénard cell. When the fluid is at rest ($\underline{\mathbf{u}} = 0$), a linear temperature profile will be established as stationary state in accordance with (2.5c). Placing the upper and lower plate at $z = \pm d/2$ this profile is given by

$$\underline{T}_{cond}(z) = \underline{T}_0 - \frac{\Delta\underline{T}}{d}\,z \quad . \tag{2.6}$$

with the temperatures at the lower and upper plates being $\underline{T}_{\rm lower} = \underline{T}_0 + \Delta\underline{T}/2$ and $\underline{T}_{\rm upper} = \underline{T}_0 - \Delta\underline{T}/2$ respectively.

To determine $\underline{C}_{cond}$ we rewrite (2.5e) in the form $\underline{d}_t\underline{C} = D\nabla\cdot\underline{\mathbf{j}}_c$ with the concentration current

$$\underline{\mathbf{j}}_c = \left(\nabla\underline{C} + \frac{k_{T,0}}{\underline{T}_0}\left[1+\gamma(\underline{T}-\underline{T}_0)\right]\nabla\underline{T}\right) \quad , \tag{2.7}$$

which has to vanish in the conductive state for impermeable plates. Using (2.6) and integrating yields

$$\underline{C}_{cond}(z) = \underline{C}_0^* + \frac{k_{T,0}}{\underline{T}_0}\,\frac{\Delta\underline{T}}{d}\,z - \frac{1}{2}\frac{k_{T,0}}{\underline{T}_0}\gamma\left(\frac{\Delta\underline{T}}{d}\,z\right)^2 \quad . \tag{2.8}$$

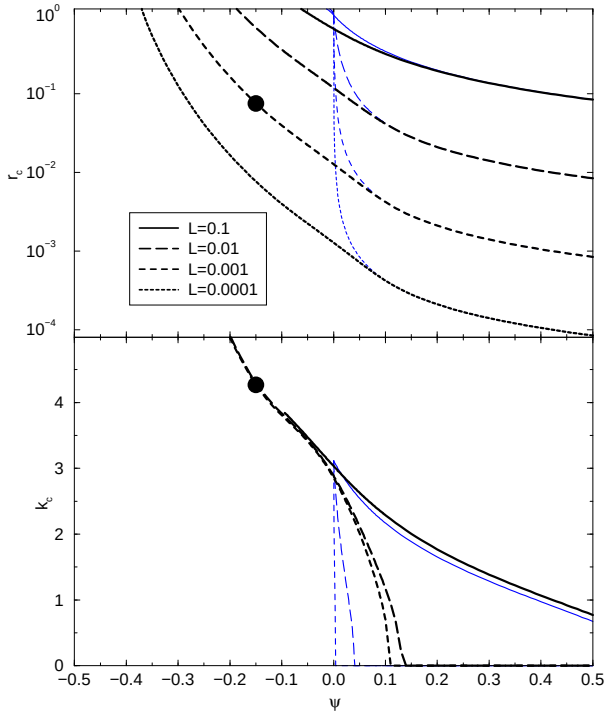

FIG. 1. (color online) The values (r_c, k_c) for heating from below and stationary convection as a function of $\overline{\psi}$ for four different L and $A = 1$ (thick black lines) compared to $A = 0$ (thin blue lines). The two dots denote the location of the structure in Fig. 2 in parameter space. The curves of k_c for $L = 0.001$ and $L = 0.0001$ would lie almost on top of each other for both values of A. k_c is thus not plotted for $L = 0.0001$.

The concentration profile is parabolic, not linear as for a temperature–independent Soret effect. The integration constant $\underline{C}_0^*$ is equal to the mean concentration $\underline{C}_0$ only for $\gamma = 0$.

$\underline{C}_{cond}(z)$ has an extremum inside of the cell if

$$\frac{\gamma d}{\Delta \underline{T}} \in \left]-\frac{1}{2}, \frac{1}{2}\right[\quad , \tag{2.9}$$

in which case $1 + \gamma(\underline{T} - \underline{T}_0)$ and thus according to (2.3) also k_T changes sign inside of the cell. When starting with a homogeneous concentration field one component will then move away from *both* the upper and the lower plate and accumulate somewhere in between.

The pressure in the conductive state can be derived from (2.5b) but the exact form is not relevant. We note that it is given by a third order polynomial of z instead of a second order polynomial as for a temperature independent Soret effect.

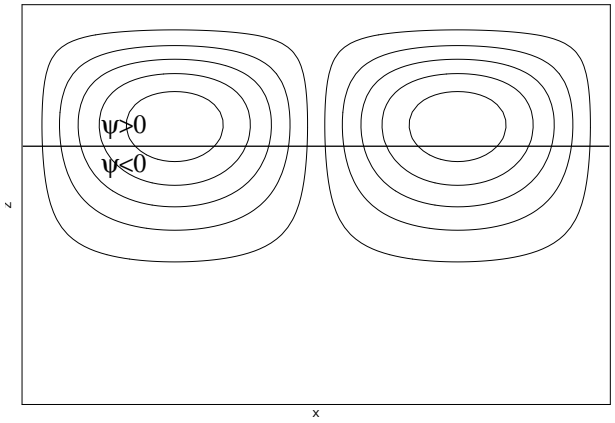

FIG. 2. The streamlines of the critical perturbation at $L = 0.001$, $\overline{\psi} = -0.15$, and $A = 1$, the point denoted in Fig. 1. The vertical line is where $\psi(T)$ changes sign in the ground state.

C. Dimensionless equations

Switching from the fields to their deviations from the ground state:

$$\underline{P} = \underline{p} - \underline{p}_{cond} \ , \qquad \underline{c} = \underline{C} - \underline{C}_{cond} \ , \qquad \underline{\theta} = \underline{T} - \underline{T}_{cond} \ , \tag{2.10}$$

we arrive at a new set of basic equations:

$$\nabla \cdot \underline{\mathbf{u}} = 0 \tag{2.11a}$$

$$\underline{d}_t \underline{\mathbf{u}} = -\nabla \frac{\underline{P}}{\rho_0} + \nu \nabla^2 \underline{\mathbf{u}} + g\left(\alpha \underline{\theta} + \beta \underline{c}\right) \mathbf{e}_z \tag{2.11b}$$

$$\underline{d}_t \underline{\theta} = \underline{w} \frac{\Delta \underline{T}}{d} + \kappa \nabla^2 \underline{\theta} \tag{2.11c}$$

$$\begin{aligned} \underline{d}_t \underline{c} = &-\underline{w} \frac{k_{T,0}}{\underline{T}_0} \frac{\Delta \underline{T}}{d} + \underline{w} \frac{k_{T,0}}{\underline{T}_0} \gamma \left(\frac{\Delta \underline{T}}{d}\right)^2 z + D \nabla^2 \underline{c} \\ &+ D \frac{k_{T,0}}{\underline{T}_0} \nabla^2 \underline{\theta} + \frac{D k_{T,0} \gamma}{\underline{T}_0} \left[\left(\underline{\theta} - \frac{\Delta \underline{T}}{d} z \right) \nabla^2 \underline{\theta} \right. \\ &\left. + \nabla \underline{\theta} \cdot \nabla \underline{\theta} - 2 \frac{\Delta \underline{T}}{d} \partial_z \underline{\theta} \right] \ . \end{aligned} \tag{2.11d}$$

$\underline{w}$ is the z–component of $\underline{\mathbf{u}}$.

To put them into a dimensionless form we use d as length scale, d^2/κ as time scale, and thus κ/d as velocity scale. Pressure, temperature, and concentration are dedimensionalized with $\rho_0 \kappa^2/d^2$, $\nu\kappa/\alpha g d^3$, and $\nu\kappa/\beta g d^3$ respectively. The dimensionless quantities are written without underscore:

$$\nabla \cdot \mathbf{u} = 0 \tag{2.12a}$$

$$d_t \mathbf{u} = -\nabla P + \sigma \left[(\theta + c) \, \mathbf{e}_z + \nabla^2 \mathbf{u} \right] \tag{2.12b}$$

$$d_t \theta = R \, w + \nabla^2 \theta \tag{2.12c}$$

$$\begin{aligned} d_t c = &R \left(\overline{\psi} + Az\right) w + LA \left(\frac{1}{R} \nabla \theta \cdot \nabla \theta - 2 \partial_z \theta \right) \\ &+ L \left[\nabla^2 c - \left(\overline{\psi} + Az - \frac{A}{R} \theta \right) \nabla^2 \theta \right] . \end{aligned} \tag{2.12d}$$

with $d_t = \partial_t + \mathbf{u}\cdot\nabla$. Five parameters appear in these equations, four of which are well known: the Rayleigh number $R = \frac{\alpha g d^3}{\nu\kappa}\Delta\underline{T}$ is the dimensionless temperature difference between upper and lower plate. The separation ratio $\overline{\psi} = -\frac{k_{T,0}\beta}{\underline{T}_0\alpha}$ measures the mean Soret effect in the conductive state. The Prandtl number $\sigma = \frac{\nu}{\kappa}$ and the Lewis number $L = \frac{D}{\kappa}$ are the dimensionless timescales of momentum and concentration diffusion respectively, i.e. relative to the chosen basic time scale of thermal diffusion. The fifth parameter A is new and describes the temperature dependence of the Soret effect. Defining $\psi(T) = -\frac{k_T(\underline{T})\beta}{\underline{T}\alpha}$ one sees that

$$A = \gamma\Delta\underline{T}\frac{k_{T,0}\beta}{\underline{T}_0\alpha} = \psi(\underline{T}_{\rm upper}) - \psi(\underline{T}_{\rm lower}) \ . \qquad (2.13)$$

By setting $A = 0$ one does of course regain the basic equations for a temperature–independent Soret effect as they can be found e. g. in [4]. Some of the modifications in (2.12d) can be easily understood. In the second term on the right hand side, $\overline{\psi}$ is for $A \neq 0$ replaced by the local, temperature–dependent separation ratio

$$\psi(T) = \psi(z,\theta) = \overline{\psi} + Az - \frac{A}{R}\theta \ . \qquad (2.14)$$

Note that $\overline{\psi}$ is in general not the average of $\psi(T)$ over the convection cell, since the average of θ need not be zero, generally. The first term describes the advective transport of the conductive state contribution to C for the space dependent separation ratio

$$-\mathbf{u}\cdot\nabla C_{cond}(z) = R\,\psi(z,\theta=0)w = R\,(\overline{\psi} + Az)w \ . \qquad (2.15)$$

Only the physical meaning of third term on the right hand side of (2.12d) is less intuitive; it stems from the application of the gradient operator to k_T/T in (2.1d).

III. BOUNDARY CONDITIONS AND NUMERICAL DETAILS

We have used the Galerkin method to simulate convection structures in this modified Rayleigh–Bénard system. To investigate $2\pi/k$–periodic, two–dimensional patterns all fields X are expanded into a sum

$$X(x,z;t) = \sum_{mn} X_{mn}(t)e^{imkx}f_n^X(z) + c.c. \ . \qquad (3.1)$$

The $f_n^X(z)$ form a complete set of orthogonal functions that fulfill the boundary conditions at the plates. A truncated ansatz is inserted into the basic equations, and the basic equations are then projected onto the functions they were expanded into. For stationary patterns an algebraic system of equations remains, with a finite subset of the amplitudes X_{mn} as unknowns. It is solved using a multidimensional Newton–Raphson method.

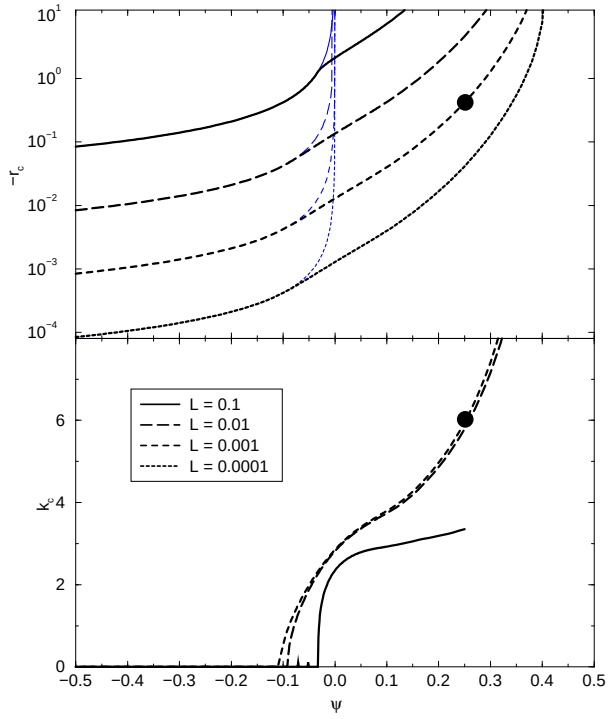

FIG. 3. (color online) The values (r_c, k_c) for heating from above as a function of $\overline{\psi}$ for four different L and $A = 1$ (thick black lines) compared to $A = 0$ (thin blue lines). The two dots denote the location of the structure in Fig. 4 in parameter space. k_c for $L = 0.0001$ is again not plotted for the same reasons as in Fig. 1. For $A = 0$ it is $k_c \equiv 0$ and therefore only the curves for $A = 1$ are shown in the lower plot.

Applying the Galerkin ansatz to the linearized equations leads to a system of first–order differential equations in time, reducing the problem of linear stability to an eigenvalue problem whose results we will discuss in Sec. IV.

We will consider the realistic no–slip impermeable boundary conditions, i. e. the complete boundary conditions read:

$$\mathbf{u} = \theta = j_{c,z} = 0 \qquad \text{at } z = \pm 1/2 \ , \qquad (3.2)$$

where $j_{c,z}$ is the z-component of the concentration current (2.7). In dimensionless form and taken at the plates where $\theta = 0$, it can be written for $z = \pm 1/2$

$$j_{c,z} = \partial_z c - (\overline{\psi} + Az)\partial_z\theta = \partial_z\left[c - (\overline{\psi} + Az)\theta\right] \ . \qquad (3.3)$$

To apply the Galerkin method it is useful to replace the concentration field c by a new field ζ defined as

$$\zeta = c - (\overline{\psi} + Az)\theta \ , \qquad (3.4)$$

such that we can write the impermeability condition as $\partial_z\zeta = 0$.

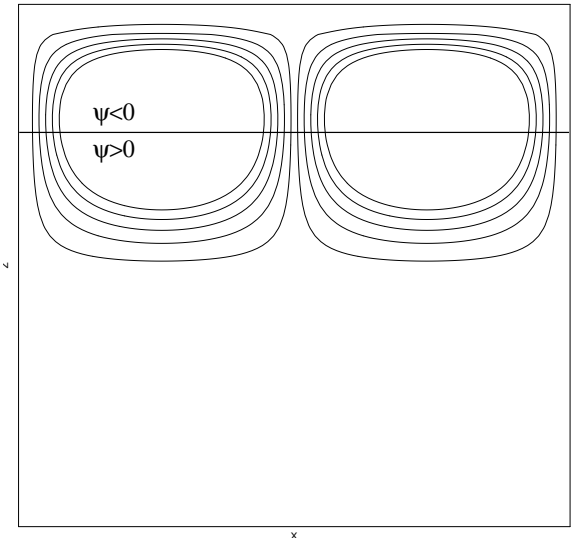

FIG. 4. The streamlines of the critical perturbation at $L = 0.001$, $\overline{\psi} = 0.25$, and $A = 1$, the point denoted in Fig. 3.

Rewriting the basic equations leads to

$$\nabla \cdot \mathbf{u} = 0 \tag{3.5a}$$
$$d_t \mathbf{u} = \sigma \left[\left([1 + (\overline{\psi} + Az)]\theta + \zeta \right) \mathbf{e}_z + \nabla^2 \mathbf{u} \right] - \nabla P \tag{3.5b}$$
$$d_t \theta = R\, w + \nabla^2 \theta \tag{3.5c}$$
$$d_t \zeta = -A\theta w - (\overline{\psi} + Az)\nabla^2\theta + L\nabla^2 \zeta + L\frac{A}{R}\left(\theta \nabla^2 \theta + \nabla\theta \cdot \nabla\theta\right) \quad . \tag{3.5d}$$

Now we define two fields Φ and Ψ via

$$\mathbf{u} = \nabla \times \nabla \times \begin{pmatrix} 0 \\ 0 \\ \Phi \end{pmatrix} + \nabla \times \begin{pmatrix} 0 \\ 0 \\ \Psi \end{pmatrix} \quad , \tag{3.6}$$

which is the most general ansatz for $\mathbf{u}$ that fulfills (3.5a) identically [27]. Taking the third component of the curl and curl curl of (3.5b) we can eliminate the pressure field and arrive at

$$\partial_t \Delta_2 \Psi = \sigma \nabla^2 \Delta_2 \Psi + \left[\nabla \times (\mathbf{u} \cdot \nabla)\, \mathbf{u}\right]_z \quad , \tag{3.7a}$$
$$\partial_t \nabla^2 \Delta_2 \Phi = \sigma \left[\nabla^4 \Delta_2 \Phi - \Delta_2 \left([1 + (\overline{\psi} + Az)]\theta + \zeta \right)\right] - \left[\nabla \times \nabla \times (\mathbf{u} \cdot \nabla)\, \mathbf{u}\right]_z \tag{3.7b}$$
$$d_t \theta = -R\Delta_2 \Phi + \nabla^2 \theta \tag{3.7c}$$
$$d_t \zeta = A\theta \Delta_2 \Phi - (\overline{\psi} + Az)\nabla^2\theta + L\nabla^2 \zeta + L\frac{A}{R}\nabla \cdot (\theta\, \nabla\theta) \tag{3.7d}$$

with $\Delta_2 = (\partial_{xx} + \partial_{yy})$.

To investigate stationary roll solutions as we will do in Sec. V, the amplitudes X_{mn} can be chosen to be real, i.e. fields Φ, θ, and ζ can be expanded laterally into $\cos(mkx)$. The amplitudes are furthermore time–independent. Ψ is not needed for 2D–structures. The boundary conditions for the new fields are, including Ψ for completeness,

$$\Phi = \partial_z \Phi = \Psi = \theta = \partial_z \zeta = 0 \qquad \text{at } z = \pm 1/2 \quad . \tag{3.8}$$

All fields except Φ can thus be expanded vertically into trigonometric functions. We expanded Φ into Chandrasekhar functions [28].

Travelling waves (TWs) will be studied in Sec. VI. In this case the amplitudes X_{mn} are generally complex and have a time dependence $X_{mn} \sim e^{\pm im\omega t}$ where the plus (minus) sign holds for left–(right–)travelling waves. TWs exhibit a x–independent mean flow $u_{\rm mf}(z)\mathbf{e}_x$ in the velocity field which is not captured by the ansatz (3.6) if

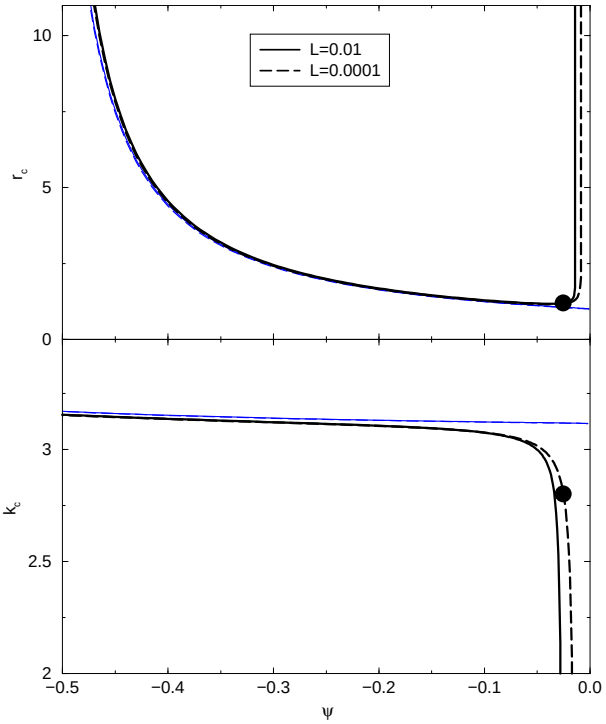

FIG. 5. (color online) The values (r_c, k_c) for heating from below and oscillatory convection as a function of $\overline{\psi}$ for $\sigma = 10$, two different L and $A = 1$ (thick black lines) compared to $A = 0$ (thin blue lines). The two dots denote the location of the structure in Fig. 6 in parameter space.

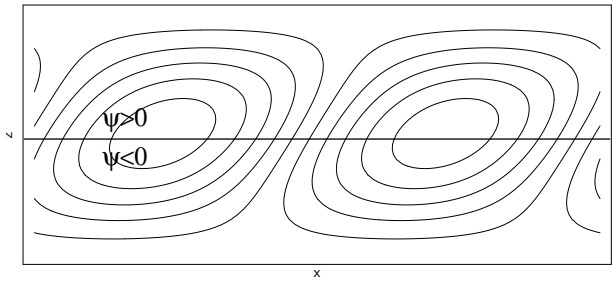

FIG. 6. The streamlines at $L = 0.001$, $\overline{\psi} = -0.025$, $\sigma = 10$, and $A = 1$, the point denoted in Fig. 5, in the laboratory frame.

one wants to stick to an expansion of the form (3.1). For TWs, we separated the mean flow component from the remaining velocity field and used (3.6) only for the latter. An additional equation for the mean flow is obtained by laterally averaging the x–component of the Navier–Stokes equation. It is

$$\partial_t u_{\rm mf} = -\left\langle (\mathbf{u}\cdot\nabla)\, u_x \right\rangle_x + \sigma\nabla^2 u_{\rm mf} \tag{3.9}$$

assuming there is no nonvanishing average lateral pressure gradient. $\langle ... \rangle_x$ denotes the lateral averaging procedure. $u_{\rm mf}$ was expanded as in (3.1) with $m \equiv 0$. We chose again Fourier modes for the expansion in z–direction.

For $A = 0$ the basic equations fulfill an up–down mirror symmetry. When $X(x,z;t)$ is a solution, so is $\pm X(x,-z;t)$, where the plus sign holds for Ψ and $u_{\rm mf}$. It turns out that the structures that first bifurcate out of the ground state are even mapped onto itself by this operation, when additionally translated by half a period (mirror–glide symmetry)[15]. As a numerical consequence, half of the amplitudes X_{mn} that belong to modes that would break this symmetry are not needed when calculating the fixed points.

For $A \neq 0$ the mirror symmetry does not hold anymore, and all amplitudes are needed to calculate the fixed points. The operation $z \to -z$, $X \to \pm X$, *and* $A \to -A$ however is still a symmetry operation, and the investigation of the model can thus be restricted to positive A. So the structures that first bifurcate out of the ground state break the mirror–glide symmetry, but performing this operation yields corresponding solutions for $-A$. In particular, the stability threshold of the ground state is independent of the sign of A.

In the truncation procedure we used, all amplitudes in (3.1) with $m + n > N_X$ were set to zero, where for the cutoffs N_X for the different fields X the relationships $N_\theta = N_\zeta = 2N_\Phi = 2N_{u_{mf}}$ hold. We used models up to $N_\theta = 40$ although in most cases models with $N_\theta = 20$ already gave quantitatively good results. In the plots presented in this paper the differences between these two models were as small or smaller than the line thickness.

IV. LINEAR STABILITY

Reintroducing $w \equiv -\Delta_2\Phi$ the linearized equations read

$$\sigma^{-1}\partial_t\nabla^2 w = \nabla^4 w + \Delta_2\left\{[1 + (\overline{\psi} + Az)]\theta + \zeta\right\} \tag{4.1a}$$

$$\partial_t\,\theta = R\,w + \nabla^2\,\theta \tag{4.1b}$$

$$\partial_t\,\zeta = -(\overline{\psi} + Az)\nabla^2\theta + L\nabla^2\,\zeta\ . \tag{4.1c}$$

The equation of motion for Ψ is not needed since it decouples and shows only decay to zero. Note that the Prandtl number enters only on the left hand side of (4.1a). The value of σ is thus at the stability threshold only important for oscillatory perturbations. The new parameter A changes the equations only insofar as $\overline{\psi}$ is replaced by $\overline{\psi} + Az$ which is the z–dependent separation ratio $\psi[T_{\rm cond}(z)]$ of the ground state.

When discussing the linear stability of the ground state for $A = 0$, three different cases have to be considered, namely stationary and oscillatory instabilities for heating from below, and stationary instabilities for heating from above. We will discuss these three cases and the changes that happen for $A \neq 0$ separately. We take $A = 1$ as an example. We also investigated other values of A but did not find any qualitative differences. Quantitatively, the deviations from the case $A = 0$ seem to grow monotonously with A. For the case $A = 0$, see [29].

A. Stationary instabilities for $R > 0$

The first instability for pure fluids appearing at a critical Rayleigh number of $R_c^0 = 1707.762$ is a stationary one. The critical perturbations have a wave number of $k_c^0 = 3.116$ [30].

The location of the critical point (r_c, k_c) as a function of $\overline{\psi}$ is compared in Fig. 1 for $A = 0$ (thin lines) and $A = 1$ (thick lines) and four values of L. For liquid mixtures typically $L \ll 1$, since the concentration diffusion is slow compared to the thermal diffusion. This is especially true for colloids, due to their large particle size. The range $-0.5 \le \overline{\psi} \le 0.5$ is the most interesting one, since for $A = 1$ ψ then changes its sign within the cell. r_c is the reduced Rayleigh number R_c/R_c^0.

Let us first discuss the constant Soret effect. A positive Soret effect increases the density gradient and thus destabilizes the layer. The convective threshold lies always below R_c^0, especially when the concentration diffusion is slow such that concentration perturbations have time to grow before they are diffused away. For negative $\overline{\psi}$ on the other hand the critical Rayleigh number is always larger than R_c^0 and even diverges quickly when $|\overline{\psi}|$ grows. For small L the divergence happens virtually directly at $\overline{\psi} = 0$ on the scales we are discussing here.

This is different when a temperature–dependent Soret effect is considered. For $A = 1$ bifurcation thresholds exist at $r < 1$ in a wide range of negative $\overline{\psi}$. For positive $\overline{\psi}$, on the other hand, the threshold becomes quickly identical to that for $A = 0$.

Changes for the critical wave number k_c are also apparent. For $A = 0$ and $L \ll 1$, k_c drops quickly from the value k_c^0 of the pure fluid to zero. This also happens for $A = 1$, but the value $k_c = 0$ is reached somewhat later. For negative $\overline{\psi}$, where no bifurcation threshold exists anymore for $A = 0$, k_c assumes for $A = 1$ values larger than k_c^0.

The qualitative changes that occur when introducing the temperature–dependent Soret effect can be understood by taking a look at the streamlines of the critical perturbation.

For a temperature–independent Soret effect, $A = 0$, the velocity field can be well represented by the leading mode Φ_{11} alone in a wide range of parameters, at the

critical point and also for finite convection at not too high amplitudes. An example of a structure where the leading mode dominates can be found in the streamline plot 12 in Fig. 9 below.

Looking at the example in Fig. 2 for a roll structure at the critical point for $A = 1$ however, one observes a crucial difference: The convection does not take place in the whole cell. A bifurcation threshold still exists for $\psi(T)$ that are negative on average ($\overline{\psi} = -0.15$) because convection is mainly restricted to the upper part of the cell where $\psi(T)$ is still positive and where thus the buoyancy is sufficiently large.

The width of the convection rolls is smaller than the height of the cell, thus $k_c > \pi \approx k_c^0$. But compared to the actual height of the rolls their width is larger, as it is for positive ψ and $A = 0$, where $k_c < k_c^0$.

When $\overline{\psi}$ becomes positive for $A = 1$ the rolls soon extend over the whole height of the convection cell. The average of $\psi(T)$ over the convection rolls becomes equal to the average $\overline{\psi}$ over the whole cell, and the values for r_c and k_c approach the values for a constant Soret effect.

B. Stationary instabilities for $R < 0$

When heated from above, a convective instability in the Bénard cell is still possible when $\overline{\psi}$ is negative, such that the heavier component reaches the highest concentration at the top of the cell.

In Fig. 3 the critical point (r_c, k_c) is now plotted for this situation, for the same values of ψ, L, and A as in the last section.

The upper plot for r_c looks qualitatively like a mirror version of the respective plot in Fig. 1. For $A = 0$, r_c diverges at some $\overline{\psi} < 0$, but for $L \ll 1$ this point lies again virtually at $\overline{\psi} = 0$ on the ψ–scale displayed in Fig. 3. For $A = 1$ however bifurcation thresholds also exist for positive $\overline{\psi}$ where an instability does not occur when ψ is temperature–independent.

The behavior of r_c is easy to understand having the results for $R > 0$ in mind. Looking again at an example for the streamlines in the case $A = 1$ for parameters where no bifurcation threshold exists for $A = 0$, (Fig. 4), one again observes that convection takes place mainly in the region where $\psi(T)$ has the right sign, i. e. $\psi < 0$, which is again the upper part of the cell, where the fluid is now warmer.

Again, we found the convection rolls to penetrate the whole cell when $\overline{\psi}$ becomes small enough, and here the bifurcation threshold does not differ anymore between the cases $A = 0$ and $A = 1$, in other words, it depends only on the average $\overline{\psi}$.

The behavior of k_c, on the other hand, cannot be explained that easily. For constant ψ and heating from below one has $k_c > 0$ when $\overline{\psi}$ is not too large, and the point where k_c becomes zero merely shifts for $A \neq 0$. But for heating from above we observe a qualitative change. While k_c always vanishes when $A = 0$, $k_c > 0$ is possible for $A \neq 0$. The very large values of k_c are again reduced when compared to the actual height of the convection rolls, instead of the whole cell.

C. Oscillatory instabilities

While for $A = 0$ and negative $\overline{\psi}$ the stationary bifurcation threshold for $R > 0$ quickly diverges the ground state instead becomes unstable at a Hopf bifurcation where the solutions of traveling and standing waves bifurcate [22]. This Hopf bifurcation exists only for negative $\overline{\psi}$ and vanishes at very small $|\overline{\psi}| = O(10^{-4})$ when L is not too large [31].

A comparison of the location of the critical point for $A = 0$ and $A = 1$ can be found in Fig. 5. For oscillatory instabilities the value of σ is of importance; we chose $\sigma = 10$, a typical value for liquids. For $A = 0$, the Φ_{11}–mode alone sufficiently describes the critical perturbation in the velocity field again. I. e. the critical streamlines will again look similar to those displayed in plot 12 in Fig. 9 below. Streamlines for example parameters at $A = 1$ are shown in Fig. 6 for the case of a left–traveling wave. The additional tilt in the convection roles stems from the breaking of the up–down symmetry of the system; similar structures can be found in the paper of Knobloch and Moore [29] (Fig. 9 in that paper). In that case the symmetry breaking is due to the choice of different thermal boundary conditions at the top and bottom plate.

The location of the bifurcation point depends only weakly on L and thus only two cases $L = 0.01$ and $L = 0.0001$ are plotted in Fig. 5. The differences between the cases $A = 0$ and $A = 1$ are also small except near $\overline{\psi} = 0$, where for temperature–dependent ψ the value of k_c drops and r_c seems to diverge. So the ψ–region of existence of oscillatory structures is not extended beyond $\psi = 0$ when the Soret effect becomes temperature–dependent, as it is the case for stationary structures. The streamline plot Fig. 6 also shows no signs of retraction of the structure into the lower region where $\psi(T) < 0$. This latter feature might be due to the fact that contrary to the two cases of stationary instability discussed before convection is not hampered per se in the region of the cell with the "wrong" sign of ψ; the opposite is the case.

Comparing the figures 1 and 5 it becomes apparent that for $A = 1$ the threshold of stationary structures lies typically well below the oscillatory threshold. The TWs will be the primary convection structures only when A is small and $\overline{\psi}$ large enough such that the temperature variation of ψ is small in any case.

V. STATIONARY NONLINEAR CONVECTION

Using the Galerkin method we calculated and compared the fixed points for stationary, roll–like convection for heating from below, for different $\overline{\psi}$ and again for the

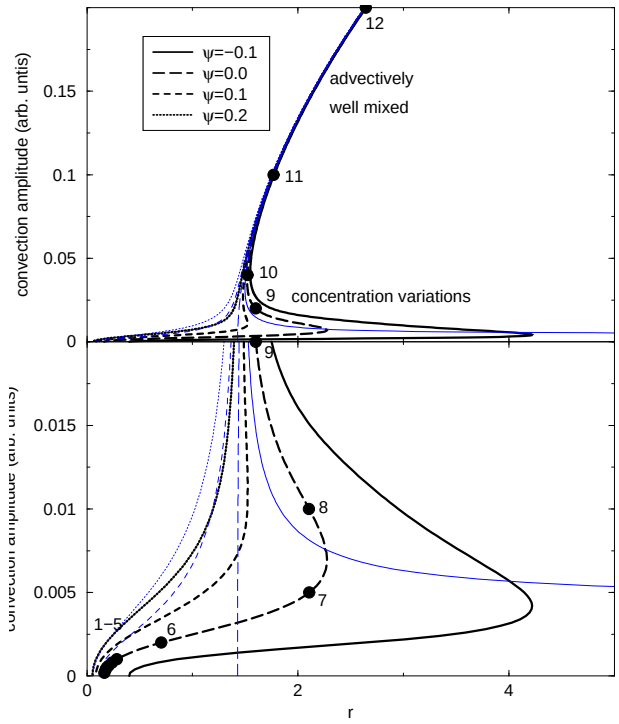

FIG. 7. (color online) A bifurcation diagram for convection rolls at $\sigma = 10$, $k = 5$, $L = 0.01$, $A = 1$ (thick, black) and $A = 0$ (thin, blue) and several values of $\overline{\psi}$. The plot below is a magnified version of the small amplitude region in the plot above. The numbered dots refer to Fig. 9.

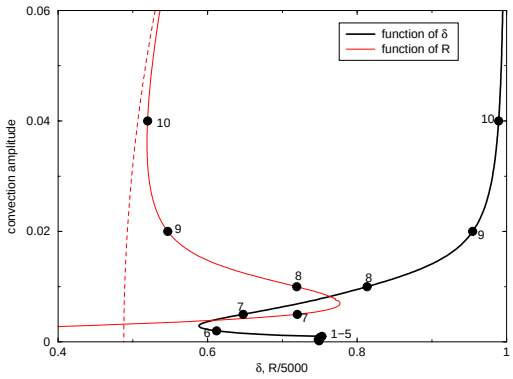

FIG. 8. (color online) The convection amplitude versus R and versus the height of the virtual cell in comparison. Parameters are $\overline{\psi} = 0$, $A = 1$, $L = 0.01$, $\sigma = 10$, and $k = 5$. The numbered dots refer to Fig. 9.

constant Soret effect $A = 0$ as well as for $A = 1$. The other parameters $\sigma = 10$, $L = 0.01$, and $k = 5$ are kept fixed in this section. The latter value was chosen to reflect the fact that $k_c(A = 1)$ assumes somewhat higher values than $k_c^0 = 3.116$ in the interesting region $\overline{\psi} < 0$.

A. Bifurcation diagrams

In Fig. 7 bifurcation diagrams are shown for both positive and negative mean $\overline{\psi}$. For large convection amplitudes, the value of $\overline{\psi}$ has very weak influence on the convection amplitude as can be seen in the upper plot. Here, the advective mixing is efficient enough to equilibrate the concentration such that a fluid with a temperature–independent $\overline{\psi} \neq 0$ behaves like a pure fluid ($\overline{\psi} = 0$). It is thus not surprising that a temperature–dependence of ψ shows no effect either.

This changes however when the convection amplitude becomes smaller and the advective mixing thus less effective. This region is shown again in the magnified lower plot in Fig. 7.

Let us first discuss the case $A = 0$. Before reaching the stability threshold $r(k = 5) \approx 1.5$ of a pure fluid ($A = 0$, $\overline{\psi} = 0$), the bifurcation curves for $\overline{\psi} > 0$ bend towards smaller r until they reach their bifurcation point at $r \ll 1$. For $\overline{\psi} = -0.1$ on the other hand the curve turns around at a saddle node, and never reaches the abscissa because r_c has already diverged for this value of $\overline{\psi}$.

For $A = 1$ the situation looks much different. Only the curve for $\overline{\psi} = 0.2$ does still qualitatively agree with its counterpart for $A = 0$. All other curves now posses two saddle nodes allowing up to three different solutions for a given r. The Rayleigh number of the first saddle node becomes rapidly larger when $\overline{\psi}$ gets smaller. We also calculated a bifurcation diagram for $\psi = -0.2$ but here the lower and middle branches already extend to so large r that our mode truncation became unreliable to decide if the saddle node still exists or diverges to leave the two branches disconnected.

Before we propose an explanation for this behavior in the next section we would like to make a remark concerning A. According to its definition in (2.13), A will grow linearly with the applied temperature difference. To compare to results of an actual experiment fixing a parameter $\tilde{A} = A/r$ instead of A would be necessary. However, since the interesting range of heating rates between the onset $r_c \ll 1$ for $\overline{\psi} < 0$ and $r = \mathcal{O}(1)$ is large, fixing $\tilde{A}$ is not possible without either A becoming unrealistically large for $r = 1$ or insignificantly small at r_c. That is why we chose to keep A fixed instead. Nevertheless, for fixed $\tilde{A}$ the bifurcation structure remains qualitatively the same and up to three different branches will still be observable. Fixing e. g. $\tilde{A}$ at 0.5 for $\overline{\psi} = 0$, three different convective solutions will exist at $r = 2$ since it is $\tilde{A}r = A = 1$ here and the existence of three solutions for this parameter combination is already known from Fig. 7.

B. Rescaling and the virtual cell

We have shown in Sec. IV C that at the onset of convection the stationary structures still exist for $R > 0$ and $\overline{\psi} < 0$ when $A = 1$ because they retract into the

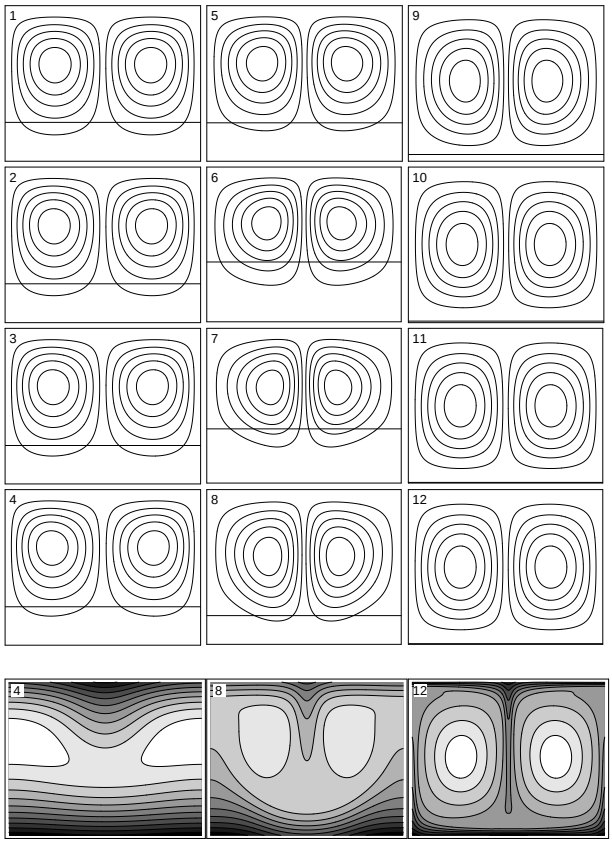

FIG. 9. Convection streamlines at the points denoted in Figs. 7 and 8. The horizontal line marks the lower end of the virtual cell. The last row shows selected concentration fields.

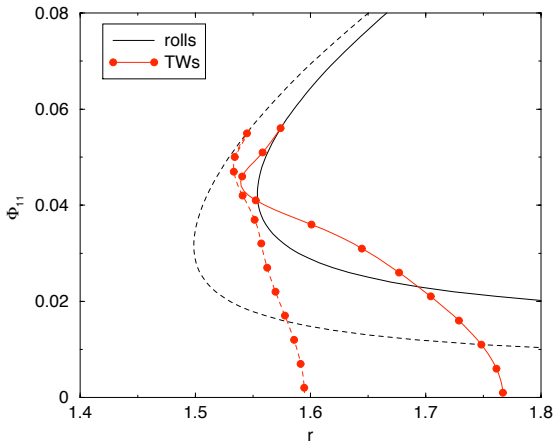

FIG. 10. (color online) The bifurcation diagrams for stationary rolls and TWs for the parameters $\sigma = 10$, $L = 0.01$, $\overline{\psi} = -0.1$, $k = 5$, and $A = 0$ (dashed) respectively $A = 1$ (solid). Dots on the TW branches denote structures with $\omega = 0$ (highest point) to $\omega = 11$ (lowest point) in steps of $\Delta\omega = 1$.

upper part of the convection cell where it is still $\psi > 0$ on average. On the other hand, inspecting the case of strong convection shows that here the convection rolls spread out over the whole cell as the concentration field becomes advectively homogenized. These two cases have to be compared with care.

In a simple model we will now assume that the convection cell is indeed less high in the case of small amplitude convection, ignoring the lower part where the fluid is still approximately at rest. Let d' be the height of the virtual cell and $\delta = d'/d$.

Parameters and fields have thus to be rescaled. The Rayleigh number R is proportional to $d^3\Delta T$ or d^4 if we only take into account the temperature difference ΔT across the virtual cell in the ground state. We therefore define a rescaled Rayleigh number $R' = \delta^4 R$. Likewise it is $k' = k\delta$. σ and L do not depend on the cell height. Finally, we define $\overline{\psi}'$ as the mean of $\psi(T_{\rm cond})$ but taken over the virtual cell only, such that $\overline{\psi}'$ can be positive when $\overline{\psi}$ is negative.

Assuming that δ is known, we can calculate the fixed point for a constant Soret effect using the five parameters R', k', $\overline{\psi}'$, σ, and L. Let $\mathbf{u}'$ be the calculated velocity field for constant $\overline{\psi}'$. On the other hand, a velocity field can also be gained directly via rescaling: With κ/d being the velocity scale it is $\mathbf{u}^{*\prime} = \mathbf{u}\delta$. Now, by comparing $\mathbf{u}^{*\prime}$ and $\mathbf{u}'$, a selfconsistent value for δ can be found. To be exact, we chose δ, such that $w^{*\prime}_{11} = w'_{11}$, where w_{11} is the amplitude of the leading mode

$$w_{11}\cos(kx)C_1(z) \tag{5.1}$$

of the w–field. $C_1(z)$ is the first Chandrasekhar function. We also tried to compare the Nusselt numbers instead, with qualitatively the same results.

The results for the reduced virtual cell height δ for $\overline{\psi} = 0$ and $A = 1$ are plotted in Fig. 8 versus the convection amplitude. For large amplitudes where the results for $A = 0$ and $A = 1$ hardly differ only a slight rescaling is needed, it is therefore $\delta \approx 1$ here. δ then shrinks as the flow becomes smaller, displaying the retraction of the convection rolls from the lower part of the cell where $\psi(T) < 0$. At even smaller amplitudes however δ becomes larger again which seems counterintuitive at first.

But comparing the values of δ (that we have found from the bifurcation diagram) with the actual streamlines as we do in Fig. 9, we see that the height of the virtual cell is actually predicted well by our scaling analysis. Especially the fact that the virtual cell grows again for the smallest convection amplitudes can actually be observed. Compare, e. g., plots 3 and 7 right next to each other. We conclude that the retraction of the rolls alone already explains the significant changes in the bifurcation curves for $A = 1$ compared to $A = 0$.

Note that the initial shrinking of the virtual cell stops between the points 6 and 7 in Fig. 8, and that also the Rayleigh number lies between this points where the pure

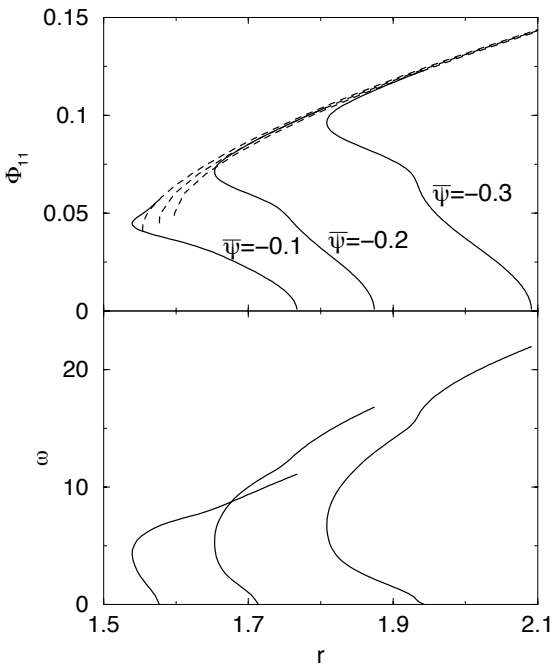

FIG. 11. The bifurcation diagrams for stationary rolls (dashed, upper branch only) and TWs (solid) for the parameters $\sigma = 10$, $L = 0.01$, $k = 5$, $A = 1$ and three different $\overline{\psi}$. Plotted are the leading Φ amplitude (above) and frequency (below) as a function of the reduced heating rate.

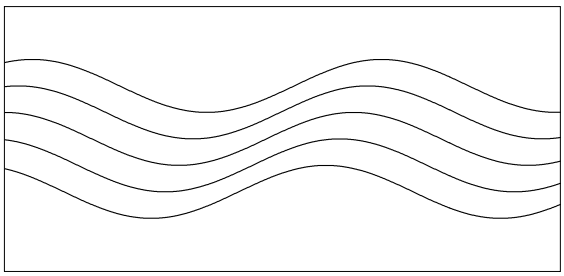

FIG. 12. A schematic picture of the streamlines in the comoving frame in the presence of a tilt in the convection rolls. The streamlines go from left to right.

fluid with $\psi(T) \equiv 0$ becomes unstable against perturbations with $k = 5$. We therefore explain the initial shrinking like that: Between point 1 and 6 the fluid layer is stable as far as only thermally caused density gradients are considered. From point 1 to 6 the fluid layer becomes more and more stabilized in the lower region where $\psi < 0$ because the stabilizing concentration gradient increases with increasing temperature difference. The convection rolls are therefore pushed out of the lower half of the cell. Only when point 7 is reached the layer has also become thermally unstable, and the stabilizing effect of the negative ψ in the lower region becomes less and less effective, especially since the convection amplitudes begin to grow quickly now, leading to a better advective mixing.

As a technical remark we would like to point out that for strongly retracted rolls and smaller k than $k = 5$ the Newton routine we used to calculate the fixed points exhibited increasing convergence problems for strongly retracted rolls. A closer inspection showed that the roll fixed point competes with another structure here in which the most important mode in the velocity field has the wave number $2k$. This is a feature familiar to us from the ordinary system with constant ψ where similar convergence problems sometimes arise for $k \approx 1.5$ or smaller. This may be interpreted as a hint that the system generally prefers structures with large k for strong retraction as the larger values for k_c already suggest.

A last feature we want to point out is that the streamlines in the middle of the cell are pushed together, best visible in the streamline plot 7 in Fig. 9. The velocity here is thus larger than at the left and right boundaries of the plot. The fluid is streaming down in the middle of the plot, as is apparent in the concentration plots in the bottom row of Fig. 9. The fluid is streaming down faster than streaming up because for streaming down concentration and temperature gradient work together. A fluid packet traveling down will be both colder than the environment and contain more of the heavier component. When traveling up it will be warmer, but its composition will be not much different since it starts its way up in an environment with $\psi \approx 0$ in the middle of the cell.

VI. OSCILLATORY NONLINEAR CONVECTION

We also calculated the TW fixed points for the same parameters $\sigma = 10$, $L = 0.01$, and $k = 5$ as in Sec. V which we will again compare for a temperature–independent Soret effect, $A = 0$, and a temperature–dependent ψ with $A = 1$.

Figure 10 shows the bifurcation diagrams of stationary rolls and travelling waves for these two cases and for a mean separation ratio of $\overline{\psi} = -0.1$. For $A = 1$ the lower forward roll branch at very small amplitudes is not shown. The mean qualitative difference is that for $A = 1$ the oscillatory branch crosses the roll branch near the second saddle and finally meets it coming from above. A temperature–dependent Soret effect delays the oscillatory instability somewhat but since we didn't find any retraction of the traveling waves into the region of negative ψ we made no attempt to express this shift of the TW branch quantitatively in terms of a virtual cell height δ.

The locations of the TW branches don't contradict the virtual cell model though. Assuming that δ is small and thus leaving k and $\overline{\psi}$ unrescaled, we can calculate δ at the onset of convection from the two critical Rayleigh numbers of the TW branches in Fig. 10 alone. It is $r_{\rm osc}(A = 1) \approx 1.77$ and $r'_{\rm osc}(A = 1) \equiv r_{\rm osc}(A = 0) \approx 1.59$ yielding $\delta \approx 0.97$ which a posteriori justifies to ignore the rescaling of k and $\overline{\psi}$. However, this δ is too close

to 1 to allow a meaningful comparison with the actual streamline plots. δ becomes even closer to 1 at higher amplitudes where the separation of the two branches is smaller.

The dots on the TW branches denote structures with frequencies $\omega = 0, 1, ...\ 11$. Despite the different position of the branches the frequencies for $A = 0$ and $A = 1$ at the same amplitudes are very similar. In particular, the branches end at approximately the same amplitude at the respective roll branches, and the Hopf frequencies differ only about a few percent.

Figure 11 shows bifurcation diagrams for $A = 1$ and three different $\overline{\psi}$. Additionally to the leading amplitudes of the Φ–field the frequencies are also plotted. Comparing to the case of temperature–independent ψ we found the TW branches for $A = 0$ and $A = 1$ to become more and more similar to each other with growing $|\overline{\psi}|$. In particular, the additional crossing of the roll branch doesn't happen anymore for larger $|\overline{\psi}|$. For the $\overline{\psi} = -0.2$ and $\overline{\psi} = -0.3$ we again found that the TW frequencies at a given amplitude depend only weakly on A.

The main qualitative feature of the convection for $A \neq 0$ is the tilt of the convection rolls already seen in Fig. 6. We found qualitatively the same pattern everywhere along the investigated TW branches with different tilt angles. The tilt is less pronounced for larger $|\overline{\psi}|$ and the angle decreases monotonously with growing amplitude and shrinking frequency along the TW branch.

It is more instructive to discuss this feature in the frame comoving with the pattern. As long as the phase velocity is large compared to the convection velocity, the streamlines will have an approximately harmonic form, described by an expression

$$z = z_0 + A(z_0)\cos(kx + \varphi) \quad . \tag{6.1}$$

The phase φ depends linearly on z in the presence of a tilt. For the left traveling wave in Fig. 6 $\partial\varphi/\partial z$ is negative. Near the center of the cell where the convection velocities are largest the streamlines on which test particles move from left to right are pushed together for upflow and pulled apart for downflow. This is shown schematically in Fig. 12. In other words, in the presence of this tilt upward movement is faster than downward movement. This is to be expected for positive A where the lighter fluid is concentrated near the center of the cell as long as $|\overline{\psi}|$ is small. For larger $|\overline{\psi}|$ the concentration maximum wanders towards the upper plate, away from the region of strongest convection in the middle of the cell. The concentration profile becomes more linear here, and the preference of upward movement less pronounced. Advective mixing also destroys this effect which explains the decrease of the tilt angle with growing amplitude.

Actual streamline plots along the TW branch for $\overline{\psi} = -0.1$ in the comoving frame are shown in Fig. 13 together with corresponding concentration plots. Note that the streamlines agree qualitatively well with isolines of the concentration, a feature that is already known from the case of temperature–independent ψ [32]. The effect of the tilt on the streamlines as shown schematically in Fig. 12 is best visible for $\omega = 3$ (left, second plot from the top).

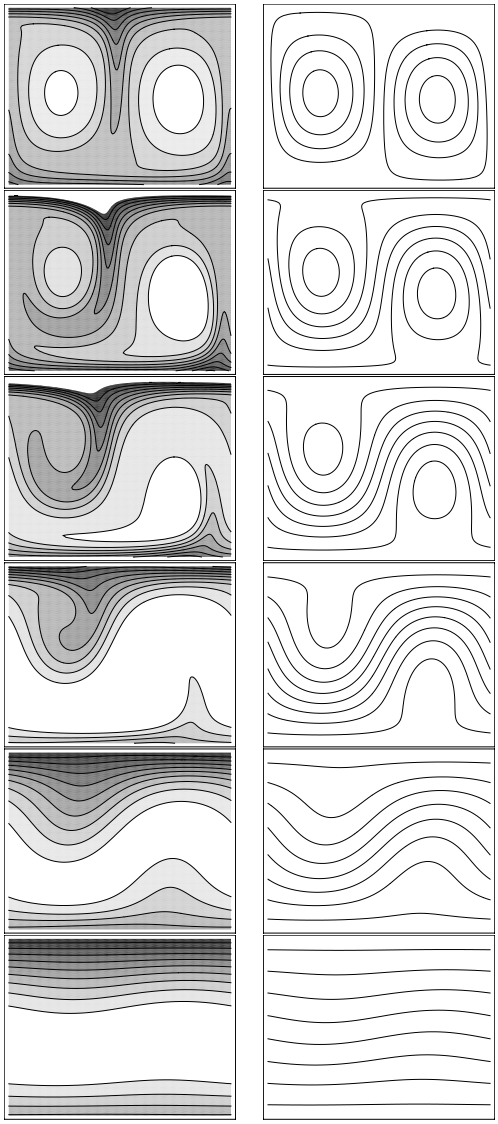

FIG. 13. Streamlines in the comoving frame (left) and the corresponding concentration field (right) for TWs at $\sigma = 10$, $L = 0.01$, $\overline{\psi} = -0.1$, $k = 5$ and $A = 1$ at frequencies $\omega = 11, 9, 7, 5, 3, 1$ (from top to bottom).

VII. CONCLUSION

In this paper we have theoretically investigated the Rayleigh–Bénard convection in binary fluids with a Soret effect that varies with the local temperature in the fluid.

Studying this temperature–variation of the Soret effect is of interest because contrary to the other material parameters it can undergo a change of sign and bifurcation diagrams for positive and negative ψ are qualitatively

significantly different. Polymer solutions exist in which the separation ratio varies significantly within a small temperature interval and also undergoes a sign change.

A T–dependence of the Soret effect leads to a nonconstant density gradient in the ground state, and therefore to an unequally strong destabilization of the upper and lower parts of the fluid layer. This leads to a lower convective threshold both in the case of heating from above and below. At first, convection structures appear only in the regions of maximal destabilization. Contrary to the case of a constant separation ratio a finite stationary convection threshold exists for heating from below (above) and significantly negative (positive) mean ψ. The critical structures then appear in the region of the cell where $\psi(T)$ is still positive (negative) on average. The critical wave number assumes high values in these cases making the first appearing convection structures also narrower, thus retaining the approximate square shape of the convection rolls.

For $\overline{\psi} < 0$ the stationary instability generally precedes the Hopf bifurcation of the traveling wave branch which are for this reason less important than for constant ψ.

The bifurcation diagrams for stationary structures look similar to those for constant ψ only if the sign of ψ changes near the plates or not at all. When a sign change happens near the center of the fluid layer the diagram is qualitatively different. Two saddle points appear, dividing the bifurcation diagram into two forward branches at small and large amplitudes and one backward branch in between.

These qualitative differences between the cases of constant and nonconstant ψ can be captured however by rescaling them according to a simple model. This model assumes a virtual cell of lesser height in which the convection takes place for a constant ψ' that is the average over this virtual cell only. The height of the virtual cell can be calculated selfconsistently and agrees well with the height of the convection rolls actually observed in full numerical calculations.

The TW branches are less affected by a temperature–dependent Soret effect. An oscillatory threshold still exists at negative mean $\overline{\psi}$ only. The TW branches are shifted towards higher Rayleigh numbers. A retraction of the patterns into the region of negative ψ was not found which is consistent with the fact that the estimated heights of the virtual cells are close to the actual cell height.

ACKNOWLEDGEMENT

This work has been supported by the Deutsche Forschungsgemeinschaft.

[1] H. Bénard, Revue générale des Sciences pures et appliquées **11**, 1261-1271 and 1309-1328 (1900)
[2] J. W. S. Lord Rayleigh, Phil. Mag. **32**, 529 (1916)
[3] M. C. Cross, P. C. Hohenberg, Rev. Mod. Phys. **65**, 851 (1993)
[4] J. K. Platten, J. C. Legros, *Convection in Liquids* (Springer, New York 1984)
[5] M. Lücke, W. Barten, P. Büchel, C. Fütterer, St. Hollinger, Ch. Jung, in: *Evolution of spontaneous structures in continuous systems* ed. by F. H. Busse, S. C. Müller. Lecture Notes in Physics **55**, 127 (Springer, Berlin, Heidelberg 1998)
[6] G. Z. Gershuni, E. M. Zhukhovitskii, *Convective Stability of Incompressible Fluids* (Keter, Jerusalem, 1976)
[7] S. J. Linz, M. Lücke, Phys. Rev. A **36**, 3505 (1987)
[8] F. H. Busse, J. Fluid Mech. **30**, 625 (1967)
[9] P. Le Gal, A. Pocheau, V. Croquette, Phys. Rev. Lett. **54**, 2501 (1985)
[10] E. Moses, V. Steinberg, Phys. Rev. Lett. **57**, 2018 (1986)
[11] E. Moses, V. Steinberg, Phys. Rev. A **43**, 707 (1991)
[12] P. Bigazzi, S. Ciliberto, V. Croquette, J. Phys. France **51**, 611 (1990)
[13] M. A. Dominguez-Lerma, G. Ahlers, D. S. Cannell, Phys. Rev. A **52**, 6159 (1995)
[14] Ch. Jung, B. Huke, M. Lücke, Phys. Rev. Lett. **81**, 3651 (1998)
[15] B. Huke, M. Lücke, P. Büchel, Ch. Jung, J. Fluid Mech. **408**, 121 (2000)
[16] R. W. Walden, P. Kolodner, A. Passner, C. M. Surko, Phys. Rev. Lett. **55**, 496 (1985)
[17] D. Bensimon, P. Kolodner, C. M. Surko, H. Williams, V. Croquette, J. Fluid Mech. **217**, 441 (1990)
[18] P. Kolodner, Phys. Rev. A **46**, 6452 (1992)
[19] P. Kolodner, Phys. Rev. E **50**, 2731 (1994)
[20] D. Jung, M. Lücke, Phys. Rev. Lett. **89**, 054502 (2002)
[21] D. Jung, P. Matura, M. Lücke, Eur. Phys. J. E. **15**, 293 (2004)
[22] P. Matura, D. Jung, M. Lücke, Phys. Rev. Lett. **92**, 254501 (2004)
[23] D. Jung, M. Lücke, Phys. Rev. E **72**, 026307 (2005)
[24] R. Kita, G. Kircher, S. Wiegand, J. Chem. Phys. **121**, 9140 (2004)
[25] K. I. Morozov, in: *Thermal Nonequilibrium Phenomena in Fluid Mixtures*, ed. by W. Köhler and S. Wiegand. Lecture Notes in Physics **584**, 38 (Springer, Berlin, Heidelberg 2002)
[26] Ch. Jung, PhD thesis, Universität des Saarlandes (1997)
[27] R. M. Clever, F. H. Busse, J. Fluid Mech. **198**, 345 (1989)
[28] S. Chandrasekhar, *Hydrodynamic and hydromagnetic stability*, Appendix V (Dover, 1981)
[29] E. Knobloch, D. R. Moore, Phys. Rev. A **37**, 860 (1988)
[30] The critical wave number is $k_c^0 = 3.1163$. The value $k_c^0 = 3.117$ that can be found in many publications, e.g., in [28] seems to go back to the work of [33].
[31] W. Schöpf, W. Zimmermann, Phys. Rev. E **47**, 1739 (1993)
[32] St. Hollinger, PhD thesis, Universität des Saarlandes (1996)
[33] W. H. Reid, D. L. Harris, Phys. Fluids **1**, 102 (1958)